

1 **Solar occultation measurement of mesospheric ozone by**  
2 **SAGE III/ISS: Impact of variations along the line of sight**  
3 **caused by photochemistry**

4

5 **Murali Natarajan<sup>1</sup>, Robert Damadeo<sup>1</sup>, David Flittner<sup>1</sup>**

6 <sup>1</sup> Science Directorate, NASA Langley Research Center, 21 Langley Blvd., Mail Stop 401-B,  
7 Hampton, VA 23681, USA.

8 Correspondence to: Murali Natarajan ([murali.natarajan@nasa.gov](mailto:murali.natarajan@nasa.gov))

9

10 **Abstract.** Twilight gradients in the concentration of atmospheric species with short  
11 photochemical lifetimes influence the transmission data obtained in a solar occultation  
12 instrument like the Stratospheric Aerosol and Gas Experiment III aboard the International Space  
13 Station (SAGE III/ISS). These photochemically induced changes result in nonlinear asymmetries  
14 in the species distribution near the tangent altitude along the line of sight (LOS). The bias  
15 introduced by neglecting the effects of twilight variations in the retrieval of mesospheric ozone is  
16 the focus of this study. O<sub>3</sub> in the mesosphere exhibits large variations near the terminator during  
17 sunrise and sunset based on current understanding of the photochemistry of this altitude region.  
18 The algorithm used in the SAGE III/ISS standard retrieval procedure for mesospheric ozone does  
19 not include the effects of these gradients. This study illustrates a method for implementing a  
20 correction scheme to account for the twilight variations in mesospheric O<sub>3</sub> and gives an estimate  
21 of the bias in the standard retrieval. We use the results from a diurnal photochemical model

22 conducted at different altitudes to develop a database of ratios of mesospheric O<sub>3</sub> at different  
23 solar zenith angles (SZA) around 90° to O<sub>3</sub> at a SZA of 90° for both sunrise and sunset  
24 conditions. These ratios are used to scale the O<sub>3</sub> at levels above the tangent altitude for  
25 appropriate SZA in the calculation of the optical depth along the LOS. In general, the impact of  
26 the corrections due to twilight variations is to increase the contribution of the overlying layers to  
27 the optical depth thereby reducing the retrieved O<sub>3</sub> concentration at the tangent altitude. We find  
28 that at sunrise the retrieved mesospheric O<sub>3</sub> including the diurnal corrections is lower by more  
29 than 30% compared to the archived O<sub>3</sub>. We show the results obtained for different latitudes and  
30 seasons. In addition, for nearly ~~collocated~~ sunrise and sunset scans, we note that these  
31 corrections lead to better qualitative agreement in the sunrise to sunset O<sub>3</sub> ratio with the  
32 photochemical model prediction.

Deleted: collocated

## 34 1 Introduction

35  
36 The solar occultation measurement technique has been the workhorse among various methods  
37 used for monitoring the composition of the earth's atmosphere for over 4 decades. This is  
38 evidenced by many successful experiments such as SAGE, SAGE II, Halogen Occultation  
39 Experiment (HALOE), Atmospheric Trace Molecule Spectroscopy (ATMOS), Atmospheric  
40 Chemistry Experiment – Fourier Transform Spectrometer (ACE-FTS), Polar Ozone and Aerosol  
41 Measurement (POAM), SAGE III/M3M and SAGE III/ISS. Major advantages of this technique  
42 include high signal to noise ratio, high vertical resolution, and long-term accuracy provided by  
43 the 'self-calibrating' nature of the instrument operation. Limited global coverage ranks high  
44 among the disadvantages of this method. In the occultation experiments, the absorption of solar

46 radiance measured by the instrument as a function of tangent height altitude or pressure is related  
47 to the optical depth and hence the abundance of the species along the line of sight (LOS). The  
48 bulk of the absorption, in general, occurs around the tangent point because of the exponential  
49 decrease in atmospheric density with altitude and due to the slant path determined by the  
50 spherical geometry. Algorithms used in standard retrievals assume that the species distribution in  
51 atmospheric layers is homogeneous and, therefore, the variation along the LOS is symmetrical  
52 around the tangent point location. The column along the LOS is then made up of species  
53 concentrations at the tangent altitude and the layers above corresponding to a SZA of  $90^\circ$ . This  
54 assumption is quite valid for species such as  $\text{CH}_4$ ,  $\text{H}_2\text{O}$ , and stratospheric  $\text{O}_3$  because of their  
55 long photochemical lifetimes and the absence of chemically induced diurnal variations. In the  
56 case of species with short lifetimes, the sudden changes in the photolysis rates near day/night  
57 terminator trigger rapid variations in the concentration as a function of SZA. These variations  
58 result in nonlinear asymmetry along the LOS. In this case, the column along the LOS is made up  
59 of species concentration at a SZA of  $90^\circ$  at the tangent altitude and those from the layers above  
60 at SZA different from  $90^\circ$  on either side of the tangent point.

61

62 The influence of twilight variations in NO and ClO on the interpretation of solar occultation  
63 measurements was described by Boughner et al. (1980). Correction factors based on  
64 photochemical models, as discussed in the above study, have been routinely applied in the  
65 retrievals of stratospheric NO and  $\text{NO}_2$  profiles in HALOE (Gordley et al., 1996; Russell et al.,  
66 1988) and in ATMOS (Newchurch et al., 1996). Brohede et al. (2007) described the role of  
67 diurnal variations in the retrieval of  $\text{NO}_2$  from OSIRIS measurements. The algorithm used in the  
68 retrieval of  $\text{NO}_2$  in SAGE, SAGE II, SAGE III/M3M, and SAGE III/ISS neglects the twilight

69 variations. A recent study of the NO<sub>2</sub> retrieval from SAGE III/ISS by Dubé et al. (2021)

**Deleted:** Dubé et al.

70 describes the importance of considering the diurnal variations along the LOS.

71

72 Mesospheric O<sub>3</sub> is also characterized by short photochemical lifetimes and steep twilight

73 gradients and, therefore, it is a potential candidate species requiring appropriate corrections in a

74 retrieval from solar occultation instruments. Natarajan et al. (2005) noted that the diurnal

75 correction factors used in the retrieval of mesospheric ozone from HALOE (Version 19) needed

76 to be updated. They derived new factors from a diurnal photochemical model of mesospheric

77 ozone and illustrated the impact of the corrections using a small subset of retrieved HALOE

**Deleted:** and illustrated

78 mesospheric O<sub>3</sub> profiles. In the present study, we describe the application of similar corrections

79 to the SAGE III/ISS retrieval of mesospheric O<sub>3</sub>. Table 1 of the Data Product User's Guide for

80 SAGE III/ISS (2021) lists the release status of mesospheric O<sub>3</sub> data as a Beta version that is yet

81 to be validated, because it is still potentially impacted by spectral stray light within the

82 instrument. Our goal is to quantify the impact of the corrections on the archived data and to see

83 whether the changes can support other known criteria. A description of the mesospheric O<sub>3</sub>

84 variations under twilight conditions as calculated with a diurnal photochemical model is given in

85 section 2. The occultation geometry and the diurnal correction factors for mesospheric O<sub>3</sub> are

86 described in section 3. Results from the application of the factors to correct the archived data are

87 discussed in section 4. We also include the results from an approximate retrieval using the

88 archived transmission data with and without diurnal corrections. A comparison of zonally

89 averaged O<sub>3</sub> profiles with scaled data for the same period from the Microwave Limb Sounder

90 (MLS) instrument on Aura satellite is described in the next section. This is followed by a

91 discussion of sunrise to sunset mesospheric O<sub>3</sub> ratios using appropriate collocated scans and a

**Deleted:** collocated

95 comparison to theoretical values. The final summary section reiterates the importance of  
96 corrections for photochemically induced twilight mesospheric O<sub>3</sub> variations in solar occultation  
97 retrievals.

98

## 99 **2 Mesospheric O<sub>3</sub> variations at sunrise/sunset**

100

101 We use a time-dependent, one-dimensional photochemical model to obtain the diurnal variation  
102 in mesospheric O<sub>3</sub>. A detailed description of the model used in this study is given in Natarajan et  
103 al. (2005). This version of the model extends from 56 km to 100 km at 1 km intervals. The  
104 photochemical reaction scheme, shown in the appendix, includes reactions involving species  
105 from the Oxygen, Hydrogen, and Nitrogen families. Chlorine and Bromine reactions do not play  
106 a significant role in this region of the atmosphere. The adopted chemical rate constant data are  
107 from the JPL Publication 19-5 (2020). The diurnal model does not use a family approximation  
108 and reactive species O, O<sub>3</sub>, N, NO, NO<sub>2</sub>, H, OH, HO<sub>2</sub>, and H<sub>2</sub>O<sub>2</sub> are considered as independent  
109 variables. The concentrations of long-lived species are constrained by the results from a two-  
110 dimensional chemical transport model (CTM) (Callis et al., 1997). Diffusion coefficients from  
111 the CTM are used to parameterize the vertical transport. The diurnal model uses a variable time  
112 step, variable order stiff equation solver (Byrne and Hindmarsh, 1975) to integrate the system of  
113 species continuity equations. The maximum time step is 600 seconds, and the algorithm  
114 automatically reduces the time step to very low values of the order of milliseconds if needed near  
115 the terminator. The model is run for 4 diurnal cycles so that the reactive species reach a steady  
116 diurnal behavior, and the results from the fifth cycle are used in the analysis. The model is run

117 for every month at 11 latitudes, corresponding to the latitude nodes of the CTM, from 56.25° N  
118 to 56.25°S at an interval of 11.25°.

119

120 Calculated O<sub>3</sub> diurnal variation in June at the latitude of 11.25°S and at different altitudes of  
121 interest to this work is illustrated in Figure 1. We are restricting our attention to altitudes below  
122 74 km because the SAGE III/ISS O<sub>3</sub> data are noisy in the region above and the quoted  
123 uncertainty is also large. O<sub>3</sub> concentration is shown as a function of time starting at midnight.

124 Nighttime O<sub>3</sub> has a constant value representing the total odd oxygen in the lower mesosphere. A  
125 sharp decrease at sunrise is mainly caused by photolysis of O<sub>3</sub> forming atomic oxygen. The  
126 recombination of atomic oxygen and O<sub>2</sub> quickly balances the loss of O<sub>3</sub> from photolysis. This  
127 reaction is pressure dependent and becomes slower at higher altitudes. The photolysis of O<sub>2</sub>  
128 generates additional odd oxygen (O<sub>x</sub> = O + O<sub>3</sub>) and in the morning hours this leads to an increase  
129 in both O<sub>x</sub> and O<sub>3</sub>. The formation of odd hydrogen species from the reaction of O(<sup>1</sup>D) with H<sub>2</sub>O  
130 during the day triggers the catalytic destruction of odd oxygen through reactions involving OH.  
131 It is noted that between 50 and 80 km the chemical time constant of O<sub>x</sub> is of the order of few  
132 hours and O<sub>x</sub> exhibits a diurnal variation caused by the competing production and destruction  
133 reactions. In the early morning there is a net gain of O<sub>x</sub> and in the evening there is net loss of  
134 O<sub>x</sub>, which continues even after sunset until atomic oxygen is depleted. The partitioning of O<sub>x</sub>  
135 into O and O<sub>3</sub> is mainly controlled by the photolysis of O<sub>3</sub> and the production of O<sub>3</sub> through the  
136 recombination of O and O<sub>2</sub>. The large increase in O<sub>3</sub> seen around sunset is mainly due to the  
137 decrease in the photolysis of O<sub>3</sub> and the continuation of the recombination of O and O<sub>2</sub>. O<sub>3</sub>  
138 reaches a steady value within an hour or so after sunset. The diurnal model extends to 100 km;

Deleted: The upper X-axis shows the corresponding SZA.

140 however, since the quoted uncertainty above 70 km in the archived SAGE III/ISS O<sub>3</sub> is large, we  
141 will focus on the region below.

142

143 The results of the full diurnal cycle are of general interest about the model simulation. But, with  
144 reference to solar occultation measurements, the sharp gradients seen in the O<sub>3</sub> concentration  
145 near SZA of 90° are more critical. The significance of the twilight variations to the retrieval of  
146 mesospheric O<sub>3</sub> under sunrise/sunset conditions can be understood with the help of the schematic  
147 shown in Figure 2. This illustrates the occultation geometry in the plane containing the LOS.

148 The red line denotes the LOS at a tangent altitude of Z<sub>T</sub>. Points F and N represent the  
149 intersection of the LOS with an atmospheric layer at an altitude of Z shown in green. For a  
150 species with little or no twilight variations, the concentrations at the locations F and N are nearly  
151 equal to that at the location U, the tangent point at an altitude of Z. In this case, the  
152 concentrations at tangent height Z<sub>T</sub> can be derived in a straightforward manner from the  
153 measured transmission using a retrieval algorithm. However, if the photochemistry causes  
154 significant gradients near SZA of 90°, as in the case of mesospheric O<sub>3</sub>, the distribution around  
155 the tangent point becomes nonlinearly asymmetric because the concentrations at F and N depend  
156 on the respective local SZA. This variation must be incorporated in the evaluation of O<sub>3</sub> specific  
157 optical depth along the LOS.

158

159 To illustrate the impact of diurnal variations on slant-path column of O<sub>3</sub>, we selected a typical  
160 event from the SAGE III/ISS data and applied the calculated O<sub>3</sub> variations in the slant-path  
161 column evaluation. The required parameters include month, date, event type (sunrise or sunset),  
162 tangent altitude, latitude, longitude, spacecraft latitude and longitude. These data are taken from

163 the current Version 5.2 SAGE III/ISS data available from the Atmospheric Sciences Data Center  
164 (ASDC) at NASA Langley Research Center. We used the model results for June at 11.25°S  
165 latitude to get the O<sub>3</sub> at sunrise variation along the LOS corresponding to different tangent  
166 altitudes from 56 to 76 km. The latitude of the chosen SAGE III/ISS measurement is 11.35°S.

167 The O<sub>3</sub> concentration along the LOS for tangent altitude of 64 km is shown as a function of  
168 distance along the LOS relative to the tangent point in the left panel of Figure 3. The dotted line  
169 corresponds to the O<sub>3</sub> concentration along the LOS when the diurnal variations are neglected and  
170 only the values corresponding to 90° SZA from the layers above the tangent altitude are used.  
171 The solid line represents the O<sub>3</sub> including the diurnal variations at the respective altitudes. The  
172 increased O<sub>3</sub> concentrations on the instrument side of the LOS are readily seen. The ratio of the  
173 O<sub>3</sub> column along the LOS with diurnal variations to the column without the diurnal variations is  
174 shown as a function of tangent altitude in the panel on the right side. The peak difference of the  
175 order of 30% occurs in the altitude range from 61 to 72 km. Underestimation of the partial O<sub>3</sub>  
176 slant-path column from layers above the tangent altitude in the standard retrieval translates to  
177 overestimation of the retrieved O<sub>3</sub> at the tangent altitude. The bias introduced by the neglect of  
178 twilight variations can be evaluated with the help of the diurnal model results.

179  
180 The technique is to express the O<sub>3</sub> variation as a function of SZA in terms of concentration  
181 normalized to O<sub>3</sub> at SZA of 90°. Figure 4 shows the distribution of the ratio  $O_3(\theta)/O_3(\theta=90^\circ)$   
182 near sunrise as a function of SZA and altitude obtained from the model results for 11.25°S  
183 latitude in June. For a given tangent height, the total slant-path O<sub>3</sub> column comprises of partial  
184 slant-path columns corresponding to the layers at and above the tangent height. Spherical  
185 geometry dictates that the partial pathlength along the LOS is maximum for the layer

**Deleted:** results  
**Deleted:** are  
**Deleted:** The X-axis shows the distance along the LOS relative to the tangent point with positive direction towards instrument and negative direction towards the Sun. Corresponding SZAs are shown at the top.



192 immediately above the tangent height (i.e., the lowest layer) and decreases dramatically for  
193 higher layers. This, combined with decreasing O<sub>3</sub> concentration with height in the lower  
194 mesosphere, results in a total slant-path column dominated by contributions from a few layers  
195 right above the tangent point. Therefore, only a small range of SZA, say between 86° and 94°,  
196 centered at 90° are important. At 62 km the O<sub>3</sub> ratio is less than 1.0 for SZA less than 90° and it  
197 increases gradually for SZA greater than 90°. At higher altitudes, the ratio shows a much steeper  
198 increase for SZA greater than 92°. The ratio, in some cases, is even slightly larger than 1.0 at  
199 SZA less than 90°. From the occultation geometry shown in Figure 2, it is seen that as one  
200 moves away from a SZA of 90° along the LOS at any tangent altitude, the corresponding altitude  
201 layer of interest moves upwards. Figure 5 illustrates the O<sub>3</sub> twilight ratio as a function of SZA  
202 and altitude for sunset conditions for the same latitude and month. The changes in the ratio for  
203 sunset condition are smaller and more gradual especially for SZA greater than 90° compared to  
204 the sunrise case. It should be recalled that the daytime variation in the odd oxygen concentration  
205 in the lower mesosphere impacts the O<sub>3</sub> concentration differently at sunrise and sunset. The  
206 differences between the O<sub>3</sub> variations for sunrise and sunset conditions suggest that the effects on  
207 the retrievals are different for sunrise and sunset occultations. The twilight O<sub>3</sub> ratios for altitude  
208 layers above the tangent altitude can be used to get the O<sub>3</sub> concentration and hence the optical  
209 depth along the LOS more accurately.

210

211 Mesospheric O<sub>3</sub> concentrations are influenced by reactions involving HO<sub>x</sub> species and therefore  
212 the distribution of H<sub>2</sub>O used in the model is an important factor. An earlier study with HALOE  
213 mesospheric O<sub>3</sub> data (Natarajan et al. 2005) using the results from the same CTM showed that

214 ~~the monthly~~, zonal mean H<sub>2</sub>O distribution from the CTM was in good agreement with the data

Deleted: the monthly

216 taken from the UARS reference atmosphere project. Linear trend in mesospheric H<sub>2</sub>O and solar  
217 cycle response have been addressed in literature (Remsberg et al., 2018; Yue et al., 2019). Yue  
218 et al. (2019) report a trend in mesospheric H<sub>2</sub>O of the order of 4 to 6% per decade based on the  
219 data from the Sounding of the Atmosphere using Broadband Emission Radiometry (SABER) and  
220 MLS instruments. Long term variability in H<sub>2</sub>O certainly impacts the absolute level of  
221 mesospheric O<sub>3</sub>. But, for the present study, the factor of importance is the relative variation of  
222 O<sub>3</sub> very close to SZA of 90° during sunrise and sunset in the mesosphere. We have done a  
223 sensitivity study at 11.25° S in June using the diurnal model with a 25% increase in the H<sub>2</sub>O  
224 concentration. Figure 6 displays the percent change in the twilight O<sub>3</sub> ratios for sunrise shown in  
225 Figure 4. The maximum impact below 74 km is less than 20% and it is very small in the lower  
226 regions. The twilight ratio in O<sub>3</sub> is quite robust and small changes in the atmospheric parameters  
227 such as temperature and H<sub>2</sub>O do not impact this ratio much. The use of this ratio is a valid  
228 approximation in correcting the retrieval scheme.

229

### 230 **3 SAGE III/ISS Mesospheric ozone**

231

232 The Sage III/ISS instrument payload was launched in February 2017 and successfully attached to  
233 the ISS. The ISS occupies a low earth orbit at an inclination of 51.64° that provides occultation  
234 coverage of low- and mid-latitude regions. Description of the experiment and early validation of  
235 the O<sub>3</sub> measurements are given in McCormick et al. (2020) and Wang et al. (2020). More  
236 detailed information on the various wavelength channels and data used for retrieving a suite of  
237 atmospheric species including mesospheric O<sub>3</sub> are given in SAGE III Algorithm Theoretical  
238 Basis Document (ATBD, 2002) and in the SAGE III/ISS Data Products User's Guide Version

239 3.0 (2021) (DPUG). Among the three different O<sub>3</sub> profile measurements made by the instrument,  
240 the one based on short wavelengths in the Hartley-Huggins bands refers exclusively to  
241 mesospheric O<sub>3</sub>. Three Charge-Coupled Device (CCD) pixel groups (PGs 0-2) are assigned to  
242 the short wavelengths in the 280 – 293 nm range, though only one (PG 1 centered at 286 nm) is  
243 currently used for the retrieval. According to the DPUG, mesospheric O<sub>3</sub> data have not been  
244 fully validated. We also note that the uncertainty in the archived O<sub>3</sub> concentration becomes  
245 larger than 10% above 70 km and there are some spurious negative data pointing to uncertainties  
246 in the transmission. The present study focusses only on SAGE III/ISS O<sub>3</sub> in the lower  
247 mesosphere up to an altitude of 70 km even though the retrieval itself starts at 90 km. The  
248 diurnal model described in the previous section extends up to 100km. We use the Version 5.2  
249 transmission and species data obtained from ASDC at NASA LaRC. For each year and month,  
250 we have categorized the scans according to event type, sunrise, or sunset. The input data for our  
251 analysis include the tangent point latitude and longitude, spacecraft latitude and longitude,  
252 vertical profiles of neutral density, mesospheric O<sub>3</sub>, and transmission. We use only the  
253 transmission data from the science pixel group 1 (PG1), which has a center wavelength of  
254 286.124 nm, since the predominant species active in this wavelength region is O<sub>3</sub>.

255

256 We have generated a database of O<sub>3</sub> twilight ratios for sunrise and sunset conditions from the  
257 diurnal model results. These ratios cover for each month the latitude range from 56.25°N to  
258 56.25°S at an interval of 11.25°, SZA from 84° to 96° at 0.5° intervals, and altitudes from 56 to  
259 90 km at 0.5 km intervals. Using the input data from each of the SAGE III/ISS occultations and  
260 spherical geometry relations, for every tangent altitude we compute the SZA as well as partial  
261 pathlengths corresponding to overlying layers. This generates a pathlength matrix like the one

262 used in the standard retrieval. Appropriate O<sub>3</sub> twilight ratios are then obtained by interpolation  
263 using the SZA and layer altitude. Multiplication of the standard pathlength matrix by the O<sub>3</sub>  
264 ratios yields the modified pathlength matrix including the effects of diurnal variations.

265

266 The twilight ratios can either be used to modify the O<sub>3</sub> profiles from the standard retrieval or be  
267 incorporated in a new retrieval from measured transmission profile. The first method is like the  
268 procedure described by Dubé et al. (2021) for making diurnal corrections to stratospheric NO<sub>2</sub>  
269 data from SAGE III/ISS. The archived SAGE III/ISS O<sub>3</sub> profile and the standard pathlength  
270 matrix are used to recreate the O<sub>3</sub> specific slant optical depth, as shown by the equation

271 
$$\tau = \sigma S n \quad (1)$$

Deleted: n,

272 where  $\tau$  is the O<sub>3</sub> slant optical depth profile,  $\sigma$  is the O<sub>3</sub> cross section corresponding to the center  
273 wavelength of PG1, and  $n$  is the O<sub>3</sub> profile from the standard retrieval.  $S$  represents the  
274 pathlength matrix with each row corresponding to a tangent point altitude. This can be written as  
275 a triangular matrix because of the geometric symmetry on opposite sides of the tangent point as  
276 can be seen from Figure 2. The slant optical depth can then be converted to a O<sub>3</sub> vertical profile  
277 corrected for diurnal variations using the modified pathlength matrix described earlier, as shown  
278 by the equation

279 
$$n_{wd} = (S_{wd})^{-1} \tau / \sigma = (S_{wd})^{-1} S n \quad (2)$$

Deleted: (

280 where  $S_{wd}$  is the modified pathlength matrix with diurnal correction and  $n_{wd}$  is the corrected O<sub>3</sub>  
281 profile. Here it is assumed that the O<sub>3</sub> absorption coefficient remains constant along the LOS.

282 This procedure gives a quantitative estimate of the over-prediction by the standard retrieval. The  
283 results for a sunrise event on June 14, 2021 (Event ID =2021061438SR) are shown in Figure 7.

284 The left panel displays the O<sub>3</sub> concentration profiles – the solid red line is the archived data from

287 standard retrieval and the solid black line represents the profile after applying the diurnal  
288 correction ratios to the pathlength matrix. The percent difference between the standard and the  
289 modified profiles is shown by the solid line on the right panel. For this occultation, the difference  
290 exceeds 40% above 64 km. This is consistent with the change in O<sub>3</sub> slant column due to the  
291 diurnal correction shown in Figure 3. We also note that the retrieval becomes noisy in the upper  
292 altitudes as O<sub>3</sub> concentrations reach near detection limits. In the second method, instead of  
293 evaluating the slant optical depth using equation 1, the archived slant-path transmission data,  
294 which corresponds to PG1, is used along with the standard and modified pathlength matrices to  
295 retrieve the vertical O<sub>3</sub> profiles. The change in the slant-path transmission corresponding to the  
296 science CCD channel PG1 for each tangent altitude below an upper boundary of 90 km is related  
297 to the total slant optical depth made up mainly of O<sub>3</sub> absorption and Rayleigh scattering  
298 contributions. After removing the Rayleigh scattering part corresponding to the center  
299 wavelength of 286.124 nm, the slant-path O<sub>3</sub> column can be estimated using the O<sub>3</sub> absorption  
300 coefficient at this wavelength taken from Bogumil et al. (2003), which is the same database used  
301 in the SAGE retrieval algorithm. The standard and modified pathlength matrices are then used to  
302 get the vertical O<sub>3</sub> profiles without and with corrections for diurnal variations respectively. The  
303 retrieved O<sub>3</sub> profiles for the sunrise event mentioned earlier are given by the dashed lines on the  
304 left panel of Figure 7, the red color denoting the standard retrieval without diurnal corrections  
305 and the black color the modified retrieval with diurnal corrections. We have used a very simple  
306 algorithm and assumed that the transmission data corresponds to a single wavelength to simplify  
307 the calculation. The actual retrieval procedure used for the archived products may have included  
308 more refinements. The agreement between results of the two different methods is very good,  
309 both for the vertical O<sub>3</sub> profiles and for the percent differences. Results for a sunset event, closer

**Deleted:** The right panel in Figure 3 shows around 30% increase in the slant-path column between 61 and 72 km.

312 to the above sunrise event in location and within a day (Sunset event ID = 2021061515SS) are  
313 shown in Figure 8. The impact of the diurnal correction is much smaller for sunset conditions.  
314 The maximum difference between the standard and modified profiles is less than 10%. The two  
315 different procedures for incorporating diurnal effects yield very nearly same results.

316

317 We have applied the diurnal corrections following the procedure described above to all the  
318 SAGE III/ISS measurements from June 2021, categorized by the event type of sunrise or sunset.  
319 Individual O<sub>3</sub> profiles were grouped together in 11 latitude bands, 11.25° wide between 56.25°N  
320 and 56.25°S. The percent difference between the standard retrieval profile and the corresponding  
321 modified profile, defined as  $(O_3/O_{3,WD} - 1) * 100$ , was calculated and the mean for each latitude  
322 band was evaluated. The subscript WD refers to the retrieval including the diurnal corrections.

Deleted: subscript

323 Figure 9 shows the resulting distribution of the mean, which represents the over-estimation by  
324 the standard retrieval, as a function of latitude and altitude. There is a latitudinal dependence  
325 with peak values occurring near 64 km and the summer hemisphere showing smaller difference.  
326 Values higher than 100% (dark violet region) are seen in the upper altitudes of the winter  
327 hemisphere. The O<sub>3</sub> profile has a sharp gradient reaching a very low minimum in winter between  
328 and 70 and 80 km. The retrieved data in this region are very noisy and thus sometimes include  
329 negative concentrations. The percent difference between the two retrievals also displays a very  
330 noisy distribution with large values of both signs. At altitudes above 85 km, the day-night

Deleted: km, the

331 terminator occurs at solar SZA greater than 96° and O<sub>3</sub> variation around 90° is small. The bias in  
332 the standard retrieval (not shown) is also small and there is no need for diurnal correction. The  
333 distribution of percent differences for sunset measurements is shown in Figure 10. The values are  
334 much smaller as discussed earlier, since the diurnal corrections are not significant for sunset. To

337 look at the seasonal dependence of the impact of diurnal corrections on the retrieved O<sub>3</sub>, we have  
338 repeated the procedure with SAGE III/ISS data from January 2021. Figure 11 displays the results  
339 for sunrise conditions. The differences between the standard and modified retrievals are larger  
340 again in the winter hemisphere with peak values occurring near 64 km. This agrees qualitatively  
341 with Figure 11 of Natarajan et al. (2005), which showed the percent difference in retrieved  
342 HALOE sunrise O<sub>3</sub> for January 1995 with updated diurnal correction factors compared to the  
343 retrieval with HALOE version 19 correction factors. The archived HALOE version 19 retrieval  
344 used correction factors from a diurnal calculation at 61 km for all mesospheric tangent altitudes  
345 above. Since a partially corrected (version 19) retrieval was used as the basis, the contour levels  
346 are negative and smaller in magnitude.

347

#### 348 **4 Comparisons with other measurements**

349

350 It is of interest to see whether the correction to the retrieval of mesospheric ozone described  
351 above can be validated by comparisons with other independent measurements. Mesospheric  
352 ozone mixing ratios at SZA of 90° during sunrise and sunset have been measured by other solar  
353 occultation experiments like HALOE and ACE-FTS. HALOE version 19 retrievals use  
354 correction factors based on diurnal model calculation near the stratopause. An update to these  
355 correction factors was discussed in Natarajan et al. (2005) but a modified version of the full  
356 ozone dataset was not generated. As far as we know, the retrieval scheme of ACE-FTS does not  
357 use any correction for twilight variations of mesospheric ozone. It should be emphasized that  
358 comparisons with data from other solar occultation experiments do not necessarily provide a

359 robust independent validation of the need to make such corrections to reduce the bias in the  
360 measurements.

361

362 MLS aboard the Aura satellite also provides vertical profiles of O<sub>3</sub> extending into the  
363 mesosphere. MLS measurements occur twice a day, once in the early afternoon and the other  
364 past midnight. Strode et al. (2022) have used the MLS data scaled with factors derived from  
365 Goddard Earth Observing System (GEOS) model coupled with the Global Modeling Initiative  
366 (GMI) chemistry mechanism for comparisons with SAGE III/ISS O<sub>3</sub> in the stratosphere. We  
367 have done similar comparisons for a selected subset of the data in the lower mesosphere using  
368 the results from the mesospheric diurnal model described earlier. We limited our attention to the  
369 data in altitude range from 56 to 70 km. We used the information provided in the MLS-V5 data  
370 quality document (Livesey et al., 2022) to properly screen the O<sub>3</sub> data. The vertical resolution for  
371 MLS O<sub>3</sub> varies from 3 to 5.5 km in the lower mesosphere. The reported accuracy varies from 8%  
372 at 0.21 hPa to 40% at 0.02 hPa. We used the MLS V-5 O<sub>3</sub> profiles from a 11.25° latitude band  
373 centered at 11.25° S from June 13 to June 15 of 2021. The native units of MLS measurements  
374 are mixing ratios on pressure levels. We used the MLS temperature and geopotential height data  
375 to get O<sub>3</sub> concentrations on an altitude grid. We derived the mean and the standard deviation  
376 profiles for both day and night MLS measurements. Results from diurnal model calculations  
377 were used to convert MLS day and night measurements to SZA of 90 ° during sunrise and sunset  
378 conditions. Figure 12 shows the O<sub>3</sub> concentration at sunrise based on MLS night data by  
379 asterisks and that based on MLS day data by diamonds. The horizontal lines represent the  
380 standard deviations at different altitudes. We also obtained the mean and standard deviation  
381 profiles from SAGE III/ISS data the same latitude band and period in June 2021 like the selected



382 MLS data. The solid black line in the figure shows the mean sunrise profile from standard  
383 retrieval and the standard deviation is represented by the yellow color band. The dashed black  
384 line is the modified retrieval with the green band showing the standard deviation. The twilight  
385 corrections to the mesospheric O<sub>3</sub> retrieval brings the profile in better agreement with that  
386 derived from MLS day and night data. Above 68 km the MLS day measurements have large  
387 variability, and the standard deviation is larger than the mean. Figure 13 shows the comparison  
388 of the profiles for sunset conditions. The difference between the modified and the standard  
389 retrievals is much smaller for the sunset conditions compared to the sunrise condition. Overall  
390 SAGEIII/ISS mesospheric O<sub>3</sub> has a positive bias. The vertical resolution of SAGE III/ISS data is  
391 about 0.7 km which is finer than the MLS vertical resolution. We found that the application of  
392 the MLS O<sub>3</sub> averaging kernel to smooth the SAGE III/ISS data has a minimum impact on the  
393 comparison.

394

395 There have been several ground-based microwave measurements of atmospheric O<sub>3</sub> and its  
396 diurnal variations (Connor et al., 1994; Parrish et al., 2014; Sauvageat et al., 2022). The  
397 microwave radiometry (MWR) in Switzerland (Sauvageat et al., 2022) provides data temporally  
398 overlapping the SAGE III/ISS data. These data are from measurements made at 2 ground stations  
399 and they extend into the mesosphere. The vertical resolution of ground based MWR is very  
400 coarse in the lower mesosphere, about 17 km (Connor et al., 1994). Therefore SAGE III/ISS O<sub>3</sub>  
401 data should be convolved with the averaging kernels of MWR prior to comparisons. In addition,  
402 MWR provides hourly data and, unless the local measurement time coincides with SZA of 90°  
403 during sunrise and sunset, the data must be converted using factors based on diurnal model. We  
404 feel that comparison with MWR data is outside the scope of this paper.

405

406 **5 Sunrise to Sunset Ratio**

407

408 Brühl et al. (1996), in their paper on HALOE O<sub>3</sub> channel validation, discussed the sunrise to  
409 sunset differences in O<sub>3</sub> around 0.1 hPa (about 64 km). Mesospheric layers are under sunlit  
410 conditions even at SZA slightly greater than 90° at dawn and dusk. As explained earlier, the  
411 viewing geometry in solar occultation observations leads to an increase in the contribution of  
412 overlying layers to the O<sub>3</sub> optical depth because O<sub>3</sub> concentrations corresponding to varying SZA  
413 greater than 90° are seen along the LOS. We have noted that the impact is larger during sunrise  
414 than sunset measurement. The sunrise to sunset O<sub>3</sub> concentration ratio becomes larger if the  
415 diurnal variations along the LOS are not considered in the retrieval. Solar occultation  
416 experiments occasionally offer the opportunity to approximately check this ratio as a test of  
417 consistency of measurement and agreement with theory. This is possible when sunrise and  
418 sunset orbits cross over each other within a reasonably short interval of time and physical  
419 proximity. Such near coincidences are quite rare. We selected sunrise/sunset pairs of  
420 measurements by SAGE III/ISS having tangent locations within 1.5° latitude, and 15° longitude  
421 of each other and separated by a maximum of 36 hours. The effect of advection by the prevailing  
422 westerly wind requires that the time and longitude differences are in the correct direction. There  
423 are just 10 pairs of sunrise /sunset measurements in June 2021 that satisfy the above criteria, all  
424 of them in low latitudes with a mean latitude of 10.46°S at sunrise and 10.27°S at sunset. The  
425 mean of the sunrise to sunset ratios of O<sub>3</sub> concentrations for these 10 scans is shown in Figure  
426 14. The solid line corresponding to the standard retrieval shows ratios greater than 1.1 above 60  
427 km. The green color shade represents the standard deviation. The modified retrieval yields a ratio

428 shown by the dashed line decreasing from 1.01 at 60 km to lower values above. The horizontal  
429 lines are the standard deviations. The asterisk symbols represent the ratio from the diurnal  
430 model. The model value is in good agreement with the ratios from both the standard and  
431 modified retrievals near 58 km but above this altitude there is some difference. The variation  
432 with altitude in the model ratio is more like that shown by the modified retrieval. The modified  
433 retrieval qualitatively reflects the pattern that photochemistry of O<sub>3</sub> suggests in this altitude  
434 region. This comparison serves as an independent criterion to highlight the importance of  
435 including the LOS twilight variations in the retrieval of mesospheric O<sub>3</sub> in solar occultation  
436 measurements. We noticed that very few such pairs of measurements, which satisfied the criteria  
437 we have chosen, occurred during other months in SAGE III/ISS data. We have also looked at the  
438 latitudinally averaged sunrise and sunset data for June 2021 obtained for generating figures 9 and  
439 10. For the latitude band centered at 11.25° S, the sunrise to sunset ratio as a function altitude  
440 (not shown) is like Figure 14, which used only collocated data. The small sampling size of the  
441 collocated pairs of data and regions of overlapping standard deviations seen in the Figure 14  
442 make this at best an approximate comparison. Other independent measurements are needed to  
443 verify the altitude variation of the ratio of sunrise to sunset O<sub>3</sub> concentrations.

444

## 445 6 Summary

446

447 Photochemically induced changes in species concentration at twilight can cause asymmetries in  
448 the distribution along the LOS of a solar occultation observation, variations that must be  
449 considered in the retrieval algorithm. Prominent among the species that need corrections for  
450 twilight variations are NO and NO<sub>2</sub> in the stratosphere and O<sub>3</sub> in the mesosphere. The SAGE

Deleted: 14, which

Deleted: collocated

Deleted: collocated

454 III/ISS instrument uses the measurements in the short-wave Hartley-Huggins band to get  
455 mesospheric O<sub>3</sub> profiles. The standard retrieval procedure does not consider the LOS variations  
456 in O<sub>3</sub> caused by photochemistry. This study describes a procedure to use results from diurnal  
457 photochemical model simulations to develop correction factors for different altitudes, latitudes,  
458 and months. These factors were used along with the archived SAGE III/ISS mesospheric O<sub>3</sub> data  
459 for selected time periods to obtain modified O<sub>3</sub> profiles. For the month of June 2021, it is shown  
460 that neglecting the diurnal variations can result in nearly 50% overestimation of O<sub>3</sub> at 64 km at  
461 lower latitudes. An approximate retrieval using the transmission data from SAGE III/ISS also  
462 indicates similar behavior in the profiles obtained with and without diurnal corrections. The  
463 retrievals were repeated for January 2021 to study the seasonal impact. Larger differences are  
464 generally seen near 70 km in high latitude winter hemisphere, and this is most likely due to a  
465 combination of very low O<sub>3</sub> concentrations, large twilight correction factors, and large  
466 uncertainties in the data. The results from this study are in good agreement with those obtained  
467 for the retrieval of HALOE mesospheric O<sub>3</sub> data.

Deleted: nd

468  
469 SAGE III/ISS data include a few nearly ~~collocated~~ sunrise and sunset measurements, mostly in  
470 the low latitudes and about a day apart. There are 10 pairs of such sunrise and sunset  
471 measurements in June 2021. An analysis of the sunrise to sunset ratio profile from these data  
472 indicates that the retrievals that include the diurnal variations show qualitatively better agreement  
473 with theoretical prediction.

Deleted: collocated

474

475 **Data Availability**

478 SAGE III/ISS version 5.2 data is available from <https://asdc.larc.nasa.gov/project/SAGE%20III->  
479 [ISS/g3bssp\\_52](https://asdc.larc.nasa.gov/project/SAGE%20III-). MLS O<sub>3</sub> data are available from <https://disc.gsfc.nasa.gov/>. O<sub>3</sub> twilight ratios  
480 used in this study are available from the author. They can also be obtained from any diurnal  
481 photochemical model of the mesosphere.

482

#### 483 **Author Contribution**

484 MN conducted the photochemical model calculations, SAGE III/ISS O<sub>3</sub> retrievals, and the  
485 analyses described in the study, and he wrote the manuscript. RD and DF provided information  
486 and guidance on the use of SAGE III/ISS mesospheric O<sub>3</sub> data as well as comments on the  
487 manuscript.

488

#### 489 **Competing Interests**

490 The authors declare that there is no competing interest for this study.

491

#### 492 **Acknowledgements**

493 SAGE III/ISS data used in this study were obtained from the NASA Langley Research Center  
494 Atmospheric Science Data Center. MN carried out this work while serving as a Distinguished  
495 Research Associate of the Science Directorate at NASA Langley Research Center. MN thanks  
496 Ellis Remsberg for reading and commenting on the draft version of this manuscript.

497

#### 498 **References**

499

500 Bogumil, K., Orphal, J., Homann, S., Voigt, P., Spietz, O., Fleischmann, A., Vogel, M.,  
501 Hartmann, H., Bovensmann, J., Frerick, J., and Burrows, J.: Measurements of molecular  
502 absorption spectra with the SCIAMACHY pre-flight model: instrument characterization and  
503 reference data for atmospheric remote sensing in the 230-2380 nm region, *J. Photochemistry and*  
504 *Photobiology A: Chemistry*, Vol 157, No. 2-3, 167-184, 2003.

505 Boughner R. E., Larsen, J. E., and Natarajan., M.: The influence of NO and ClO variations at  
506 twilight on the interpretation of solar occultation measurements, *Geophys. Res. Lett.*, 7, 231 –  
507 234, 1980.

508 Brohede, S. M., Haley, C. S., McLinden, C. A., Sioris, C. E., Murtagh, D. P., Petelina, S. V.,  
509 Llewellyn, E. J., Bazureau, A., Goutail, F., Randall, C. E., Lumpe, J. D., Taha, G., Thomasson,  
510 L. W., and Gordley, L. L.: Validation of Odin/OSIRIS stratospheric NO<sub>2</sub> profiles, *J. Geophys.*  
511 *Res.-Atmos.*, 112, D07310, <https://doi.org/10.1029/2006JD007586>, 2007.

512 Brühl, C., Drayson, S. R., Russell III, J. M., Crutzen, P. J., McInerney, J. M., Purcell, P. N.,  
513 Claude, H., Gernandt, H., McGee, T. J., McDermid, I. S., and Gunson, M. R.: Halogen  
514 Occultation Experiment ozone channel validation, *J. Geophys. Res.*, Vol. 101, NO. D6, 10,217 -  
515 10,240, 1996.

516 [Byrne, G. D., and Hindmarsh, A. C.: A polyalgorithm for the numerical solution of ordinary](#)  
517 [differential equations, \*ACM Trans. Math. Soft.\*, 1\(1\), 71-96, 1975.](#)

518 Connor, B. J., Siskind, D. E., Tsou, J. J., Parrish, A., and Remsberg, E. E.: Ground-based  
519 microwave observations of ozone in the upper stratosphere and mesosphere, *J. Geophys. Res.*,  
520 vol 99, No. D8, 16,757-16,770, 1994.

521 Dubé, K., Bourassa, A., Zawada, D., Degenstein, D., Damadeo, R., Flittner, D., and Randel, W.:  
522 Accounting for the photochemical variation in stratospheric NO<sub>2</sub> in the SAGE III/ISS solar

523 occultation retrieval, Atmos. Meas. Tech., 14, 557 – 566, <https://doi.org/10.5194/amt-14-557->  
524 [2021](https://doi.org/10.5194/amt-14-557-2021), 2021.

525 Gordley, L. L., Russell III, J. M., Mickley, L. J., Frederick, J. E., Park, J. H., Stone, K. A.,  
526 Beavee, G. M., McInerney, J. M., Deaver, L. E., Toon, G. C., Murcray, F. J., Blatherwick, R. D.,  
527 Gunson, M. R., Abbatt, J. P. D., Mauldin III, R. L., Mount, G. H., Sen, B., and Blavier, J. F.:  
528 Validation of nitric oxide and nitrogen dioxide measurements made by the Halogen Occultation  
529 Experiment for UARS platform, J. Geophys. Res.-Atmos., 101,10241–10266, 1996.

530 JPL Publication 19-5, Chemical Kinetics and Photochemical Data for Use in Atmospheric  
531 Studies, Evaluation Number 19. [https://jpldataeval.jpl.nasa.gov/pdf/NASA-](https://jpldataeval.jpl.nasa.gov/pdf/NASA-JPL%20Evaluation%2019-5.pdf)  
532 [JPL%20Evaluation%2019-5.pdf](https://jpldataeval.jpl.nasa.gov/pdf/NASA-JPL%20Evaluation%2019-5.pdf), 2020.

533 Livesey, N. J., Read, W. G., Wagner, P. A., Froidevaux, L., Santee, M. L., Schwartz, M. J.,  
534 Lambert, A., Millan Valle, L. F., Pumphrey, H. C., Manney, G. L., Fuller, R. A., Jarnot, R. F.,  
535 Knosp, B. W., and Lay, R. R.: Earth Observing System (EOS) Aura Microwave Limb Sounder  
536 (MLS) Version 5.0x Level 2 and 3 data quality and description document, JPL D-105336 Rev B,  
537 2022.

538 McCormick, M. P., Lei, L., Hill, M. T., Anderson, J., Querel, R., and Steinbrecht, W.: Early  
539 results and validation of SAGE III-ISS ozone profile measurements from onboard the  
540 International Space Station, Atmos. Meas. Tech., 13, 1287-1297, [https://doi.org/10.5194/amt-13-](https://doi.org/10.5194/amt-13-1287-2020)  
541 [1287-2020](https://doi.org/10.5194/amt-13-1287-2020), 2020.

542 Natarajan, M., Deaver, L. E., Thompson, E., and Magill, B.: Impact of twilight gradients on the  
543 retrieval of mesospheric ozone from HALOE, J. Geophys. Res., Vol. 110,  
544 doi:10.1029/2004JD005719, 2005.

545 Newchurch, M. J., Allen, M., Gunson, M. R., Salawitch, R. J., Collins, G. B., Huston, K. H.,  
546 Abbas, M. M., Abrams, M. C., Chang, A. Y., Fahey, D. W., Gao, R. S., Irion, F. W.,  
547 Loewenstein, M., Manney, G. L., Michelson, H. A., Podolske, J. R., Rinsland, C. P., and Zander,  
548 R.: Stratospheric NO and NO<sub>2</sub> abundances from ATMOS Solar-Occultation Measurements,  
549 Geophys. Res. Lett., 23, 2373-2376., <https://doi.org/10.1029/96GL01196>, 1996.

550 Parrish, A., Boyd, I. S., Nedoluha, G. E., Bhartia, P. K., Firth, S. M., Kramarova, N. A., Connor,  
551 B. J., Bodeker, G. E., Froidevaux, L., Shiotani, M., and Sakazaki, T.: Diurnal variations of  
552 stratospheric ozone measured by ground-based microwave remote sensing at the Mauna Loa  
553 NDACC site: measurement validation and GEOSCCM model comparison, Atmos. Chem. Phys.,  
554 14, 7255-7222, [www.atmos-chem-phys.net/14/7255/2014/doi:10.5194/acp-14-7255-2014](http://www.atmos-chem-phys.net/14/7255/2014/doi:10.5194/acp-14-7255-2014), 2014

555 Remsberg, E., Damadeo, R., Natarajan, M., and Bhatt, P.: Observed responses of mesospheric  
556 water vapor to solar cycle and dynamical forcings, J. Geophys. Res., 123 (7), 3830-3843,  
557 <https://doi.org/10.1002/2017JD028029>, 2018.

558 Russell III, J. M., Farmer, C. B., Rinsland, C. P., Zander, R., Froidevaux, L., Toon, G. C., Gai,  
559 B., Shaw, J., and Gunson, M.: Measurements of Odd Nitrogen Compounds in the Stratosphere  
560 by the ATMOS Experiment on Spacelab 3, J. Geophys. Res., Vol 3, D2, 1718-1736, 1988.

561 Sauvageat, E., Barras, E. M., Hocke, K., Haeferle, A., and Murk, A.: Harmonized retrieval of  
562 middle atmospheric ozone from two microwave radiometers in Switzerland,  
563 <https://doi.org/10.5194/amt-2022-212>, 2022

564 SAGE III Algorithm Theoretical Basis Document (ATBD) Solar and Lunar Algorithm, LaRC  
565 475-00-109, Version 2.1. [https://eosps.nasa.gov/sites/default/files/atbd/atbd-sage-solar-](https://eosps.nasa.gov/sites/default/files/atbd/atbd-sage-solar-lunar.pdf)  
566 [lunar.pdf](https://eosps.nasa.gov/sites/default/files/atbd/atbd-sage-solar-lunar.pdf), 2002



567 SAGE III/ISS Data Products User's Guide, Version 3.0,  
568 <https://asdc.larc.nasa.gov/documents/sageiii-iss/guide/DPUG-G3B-2-0.pdf>, 2021.  
569 Strode, S. A., Taha, G., Oman, L. D., Damadeo, R., Flittner, D., Schoeberl, M., Sioris, C. E., and  
570 Stauffer, R.: SAGE III/ISS ozone and NO<sub>2</sub> validation using diurnal scaling factors,  
571 <https://doi.org/10.5194/amt-15-6145-2022>, Atmos. Meas. Tech., 15, 6145-6161, 2022  
572 Wang, H. J. R., Damadeo, R., Flittner, D., Kramarova, N., Taha, G., Davis, S., et al.: Validation  
573 of SAGE III/ISS solar occultation ozone products with correlative satellite and ground-based  
574 measurements, J. Geophys. Res., 125, e2020JD032430. <https://doi.org/10.1029/2020JD032430>,  
575 [2020](https://doi.org/10.1029/2020JD032430).  
576 Yue, J., Russell III, J., Gan, Q., Wang, T., Rong, P., Garcia, R., and Mlynczak, M.:Increasing  
577 water vapor in the stratosphere and mesosphere after 2002, Geophys. Res. Lett., 46, 13,452-  
578 13,460. <https://doi.org/10.1029/2019GL084973>, 2019.

579

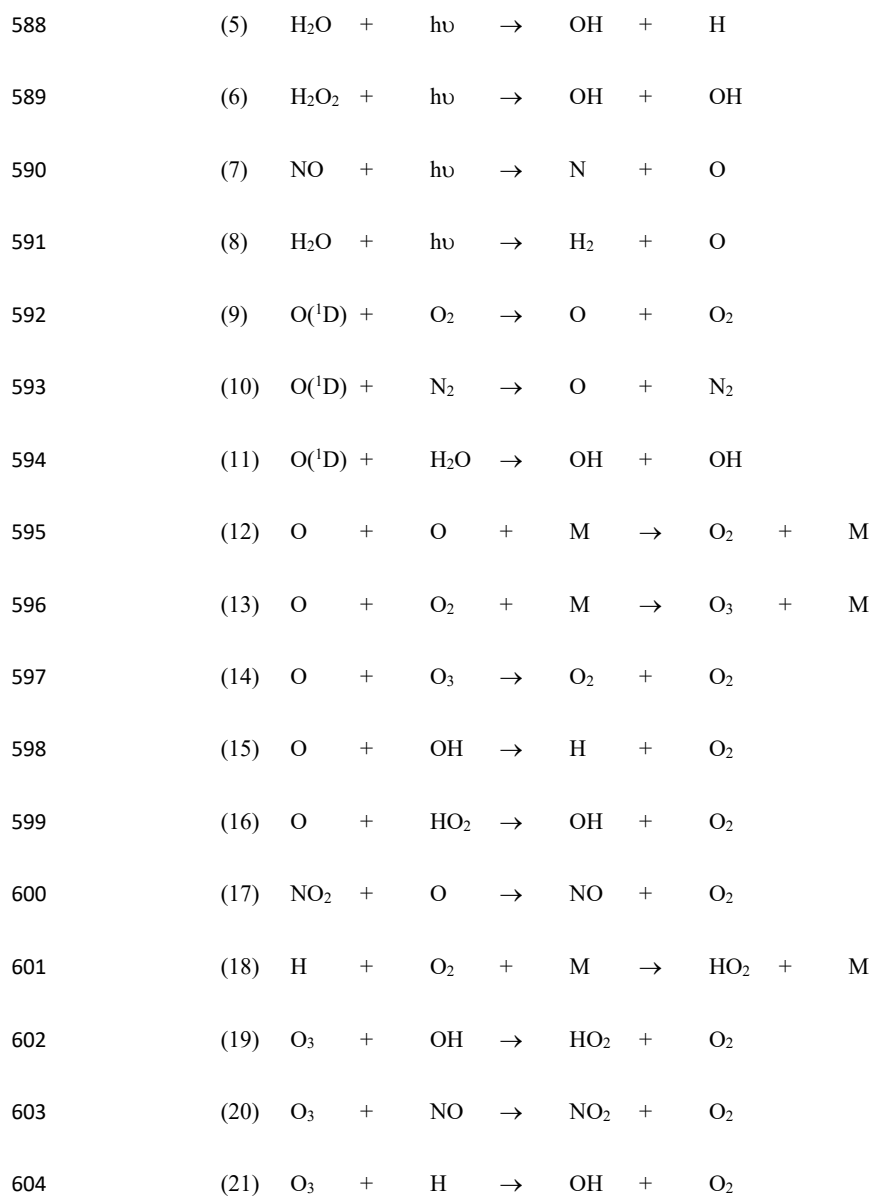
## 580 Appendix

581

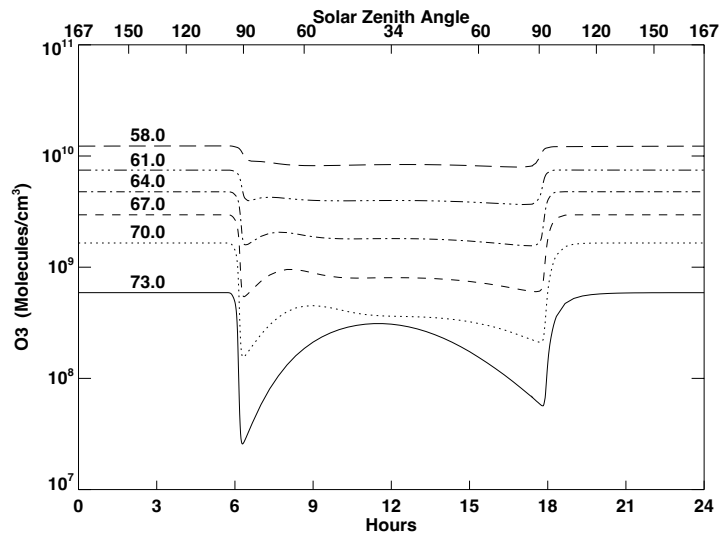
582 Photochemical reactions considered in the mesospheric diurnal model:

583





605 (22) OH + HO<sub>2</sub> → H<sub>2</sub>O + O<sub>2</sub>  
606 (23) HO<sub>2</sub> + NO → OH + NO<sub>2</sub>  
607 (24) OH + H<sub>2</sub>O<sub>2</sub> → H<sub>2</sub>O + HO<sub>2</sub>  
608 (25) HO<sub>2</sub> + HO<sub>2</sub> → H<sub>2</sub>O<sub>2</sub> + O<sub>2</sub>  
609 (26) HO<sub>2</sub> + O<sub>3</sub> → OH + 2 O<sub>2</sub>  
610 (27) O(<sup>1</sup>D) + H<sub>2</sub> → OH + H  
611 (28) N + O<sub>2</sub> → NO + O  
612 (29) N + NO → N<sub>2</sub> + O  
613 (30) N + NO<sub>2</sub> → N<sub>2</sub>O + O  
614 (31) H + HO<sub>2</sub> → OH + OH  
615 (32) H + HO<sub>2</sub> → H<sub>2</sub>O + O  
616 (33) H + HO<sub>2</sub> → H<sub>2</sub> + O<sub>2</sub>  
617 (34) OH + H<sub>2</sub> → H<sub>2</sub>O + H  
618  
619  
620

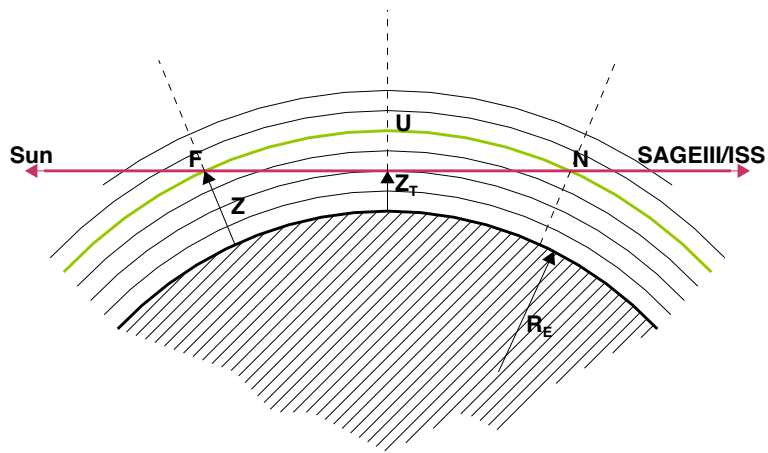


621

622

623 Figure 1. Diurnal variation in O<sub>3</sub> at 11.25°S in June at altitudes from 58 to 73 km. 0 hours

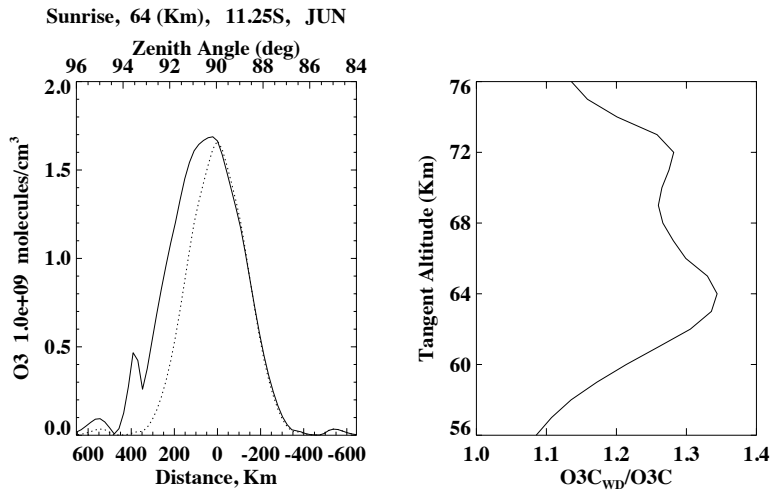
624 denote midnight. The upper X axis shows the variation of SZA.



625

626 Figure 2. Schematic representation of the solar occultation measurement.  $Z_T$  is the tangent  
 627 altitude, red line is the LOS,  $Z$  is the altitude of a layer above the tangent altitude, F (towards  
 628 sun) and N (towards SAGE III/ISS) are the points of intersection of layer at  $Z$  with the LOS, and  
 629  $R_E$  is the earth radius.

630



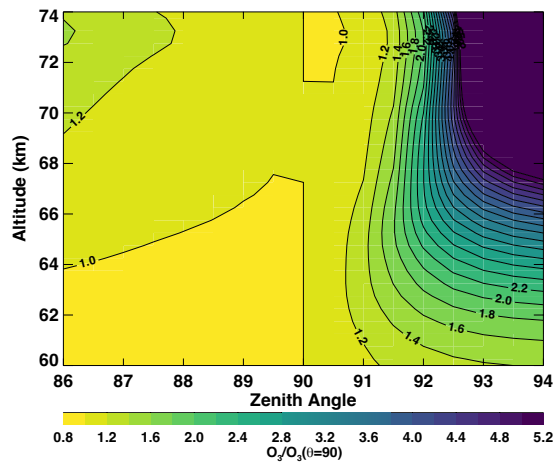
631

632 Figure 3. (Left) O<sub>3</sub> concentration along the LOS for a tangent altitude of 64 km at [sunrise](#)  
 633 [at](#) 11.25°S latitude in June. Solid line shows O<sub>3</sub> with diurnal variations and the dotted line  
 634 represents O<sub>3</sub> without diurnal variations. The X-axis represents the distance along the LOS  
 635 relative to the tangent point with positive direction towards the instrument and negative direction  
 636 towards the Sun. The upper axis shows the corresponding SZA. (Right) Ratio of the O<sub>3</sub> column  
 637 along the LOS with appropriate diurnal variations to the O<sub>3</sub> column without diurnal variations,  
 638 plotted as a function of altitude at 11.25°S in June.

639

640

641



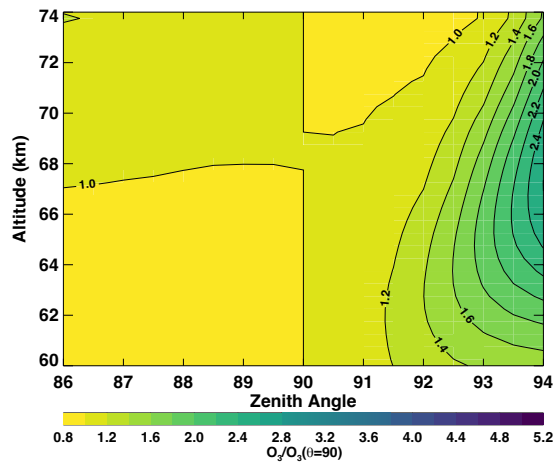
642

643 Figure 4. Ozone twilight ratio, defined as  $O_3$  at solar zenith angle  $\theta/O_3$  at  $\theta=90^\circ$ , as a function of

644 SZA and altitude for sunrise in June and 11.25°S latitude.

645

646



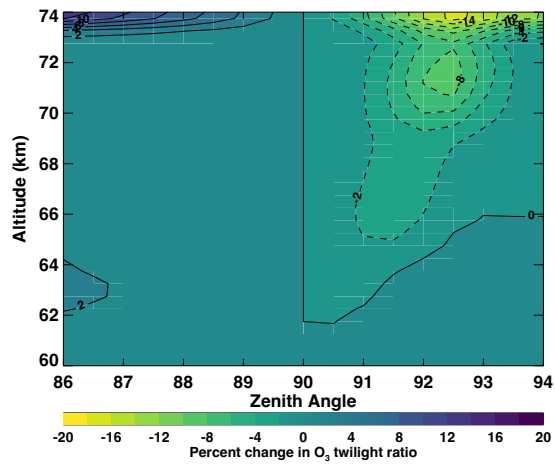
647

648 Figure 5. Ozone twilight ratio, defined as  $O_3$  at solar zenith angle  $\theta/O_3$  at  $\theta=90^\circ$ , as a function of  
 649 SZA and altitude for sunset in June and 11.25°S latitude.

Deleted: Same as Figure 4 for sunset conditions

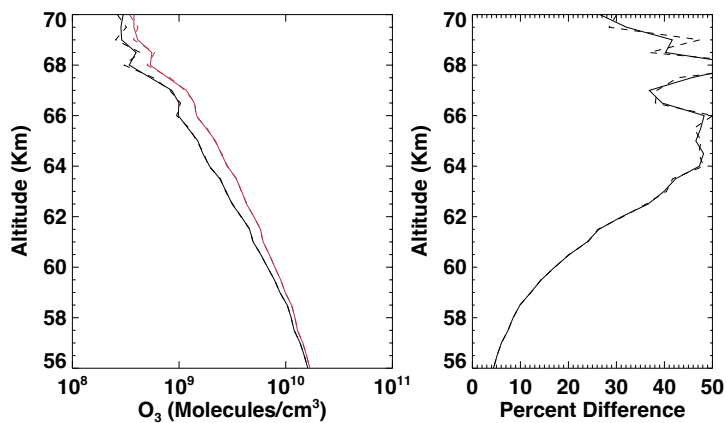
650





652

653 Figure 6. Percent change in the O<sub>3</sub> twilight ratio shown in Figure 4 when the H<sub>2</sub>O in the diurnal  
 654 model is increased by 25% at all altitudes. This figure corresponds to sunrise at 11.25° S in June.

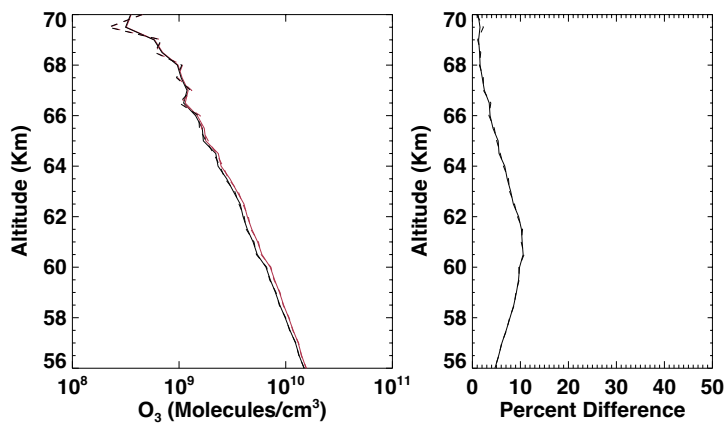


655

656 Figure 7. SAGE III/ISS  $O_3$  for a sunrise event at 11.35°S and 158.72°E on June 14, 2021 (Event  
 657 ID 2021061438SR). (Left panel) Red solid line shows the standard SAGE III retrieval, and the  
 658 black solid line represents the retrieval including the diurnal variations along LOS. The dashed  
 659 lines represent the retrievals using the transmission data, the red color for the standard retrieval  
 660 and the black denoting the retrieval with diurnal corrections. (Right panel) Percent difference  
 661 between the standard retrieval and the one with diurnal corrections; solid line using the archived  
 662 standard retrieval of  $O_3$  concentration, and the dashed line based on the approximate retrieval  
 663 using the transmission data.

664

Deleted: sunrise



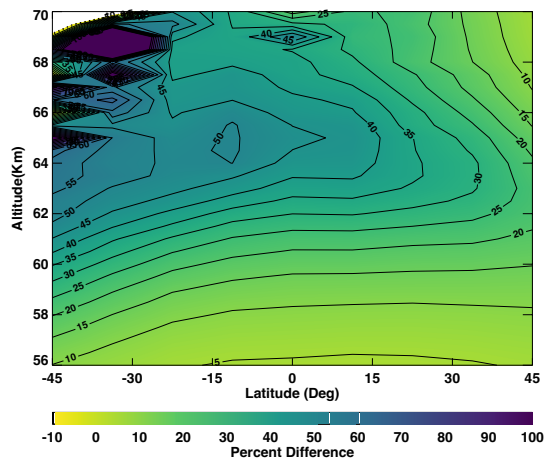
666

667 Figure 8. SAGE III/ISS O<sub>3</sub> for a sunset event at 12.05°S and 151.16°E on June 15, 2021 (Event  
 668 ID 2021061515SS). (Left panel) Red solid line shows the standard SAGE III retrieval, and the  
 669 black solid line represents the retrieval including the diurnal variations along LOS. The dashed  
 670 lines represent the retrievals using the transmission data, the red color for the standard retrieval  
 671 and the black denoting the retrieval with diurnal corrections. (Right panel) Percent difference  
 672 between the standard retrieval and the one with diurnal corrections; solid line using the archived  
 673 standard retrieval of O<sub>3</sub> concentration, and the dashed line based on the approximate retrieval  
 674 using the transmission data.

675

Deleted: Same as Figure

Deleted: 7 but for a sunset event (Event ID 2021061515SS) closer to the sunrise event shown in Figure 7.

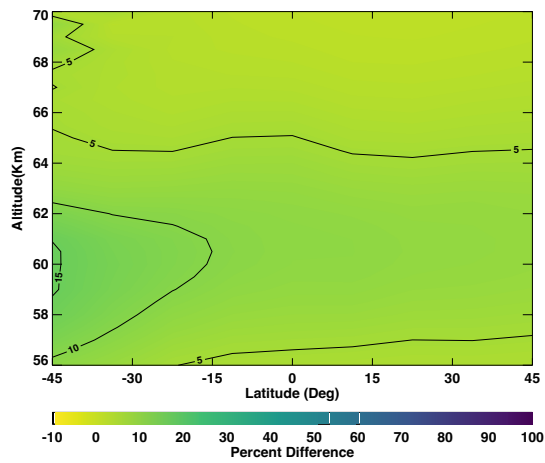


679

680 Figure 9. Latitudinal average of the percent difference in sunrise O<sub>3</sub> between the standard  
681 (archived) retrieval and a retrieval including diurnal variations along the LOS, as a function of  
682 latitude and altitude for June 2021.

683

684

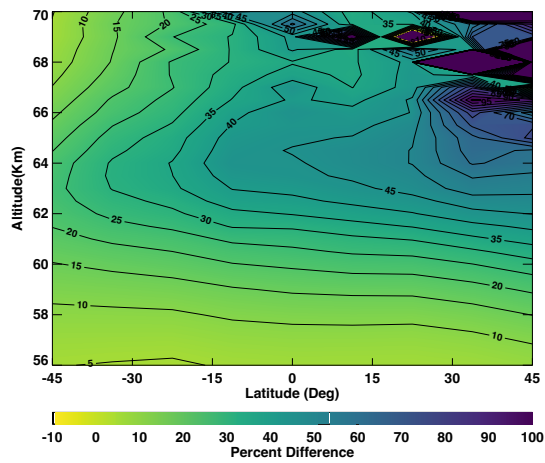


685

686 Figure 10. Latitudinal average of the percent difference in sunset O<sub>3</sub> between the standard  
 687 (archived) retrieval and a retrieval including diurnal variations along the LOS, as a function of  
 688 latitude and altitude for June 2021.

**Deleted:** Same as Figure 9 but for sunset conditions.

**Formatted:** Not Superscript/ Subscript



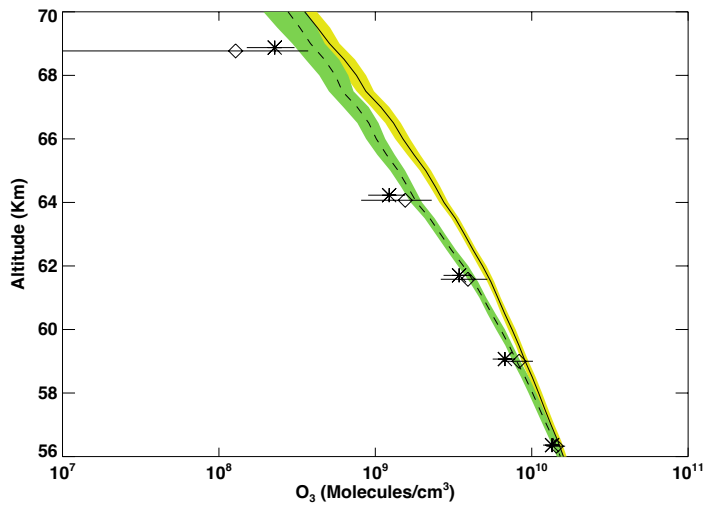
690

691 Figure 11. Latitudinal average of the percent difference in sunrise O<sub>3</sub> between the standard  
 692 (archived) retrieval and a retrieval including diurnal variations along the LOS, as a function of  
 693 latitude and altitude for January 2021.

694

695

**Deleted:** Same as Figure 9 but for January 2021.



697

698 Figure 12. Comparison of sunrise SAGE III/ISS and MLS mesospheric O<sub>3</sub> zonal mean at 11.25°

699 S in June 2021. Solid line – mean of SAGE III/ISS standard retrieval with the standard deviation

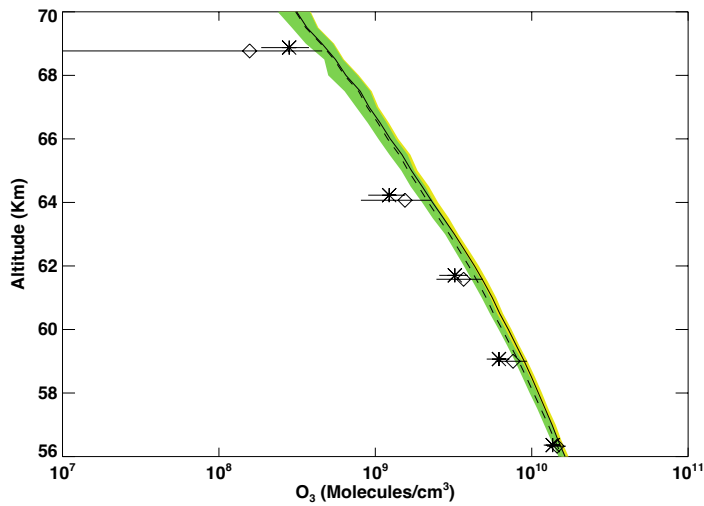
700 shown by the yellow shade; Dashed line – mean of SAGE III/ISS modified retrieval with the

701 standard deviation shown by the green shade; Asterisks – mean MLS night data scaled to

702 sunrise; Diamonds – mean MLS day data scaled to sunrise; Horizontal lines represent the

703 standard deviations.

704



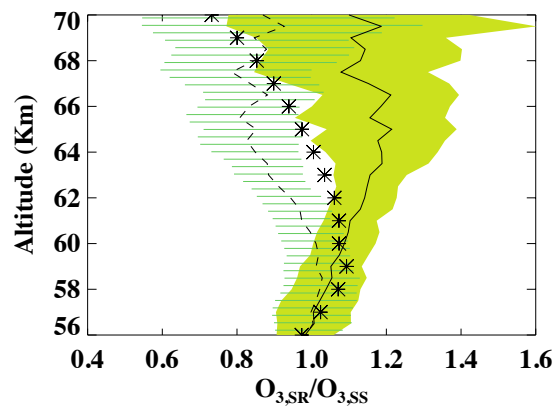
705

706 Figure 13. Comparison of sunset SAGE III/ISS and MLS mesospheric O<sub>3</sub> zonal mean at 11.25°  
 707 S in June 2021. Solid line – mean of SAGE III/ISS standard retrieval with the standard deviation  
 708 shown by the yellow shade; Dashed line – mean of SAGE III/ISS modified retrieval with the  
 709 standard deviation shown by the green shade; Asterisks – mean MLS night data scaled to sunset;  
 710 Diamonds – mean MLS day data scaled to sunset; Horizontal lines represent the standard  
 711 deviations.

712

Deleted: Same as Figure 12 but for sunset condition.





714

715 Figure 14. Vertical profile of  $O_3$  sunrise to sunset ratio in June 2021. Nearly collocated 10 pairs  
 716 of sunrises (mean latitude  $10.46^\circ\text{S}$ ) and sunsets (mean latitude  $10.27^\circ\text{S}$ ) data are used for this  
 717 plot. Solid line shows the mean ratio from standard (archived) retrieval and the green shade  
 718 represents the standard deviation; Dashed line shows the mean ratio from the retrieval including  
 719 diurnal variations along the LOS and the horizontal lines represent the standard deviation. The  
 720 asterisk symbols are the ratios from diurnal photochemical calculations at  $11.25^\circ\text{S}$  for June.